Measurements of the High-Pressure Equation of State of Deuterium

P. M. Celliers *G. W. Collins* *A. Ng**
K. S. Budil *L. B. Da Silva* *R. J. Wallace*
R. Cauble *M. E. Foord* *S. V. Weber*
D. M. Gold

Introduction

Hydrogen is the simplest and most abundant element in the universe, yet at high pressure, it is one of the most difficult to understand. Having only a single electron, it shows characteristics of both the Group I alkalis and the Group VII halogens.[1] At low pressure, hydrogen isotopes are halogenous, covalent, diatomic molecules that form insulators. With increasing pressure, the isotopes transform into alkali metals. Whereas most theories predict <300 GPa for the insulator–metal transition pressure along the 0-K isotherm,[2] static experiments at even higher pressures have not shown evidence of metallization.[3] Evidence of high conductivity was observed at an unexpectedly low pressure (140 GPa) at finite temperature (3000 K) where the isotope is in a molecular fluid phase.[4] There is no accepted theoretical description of the transformation of hydrogen from an insulator into a conducting atomic fluid at high pressures and high temperatures. This regime of high density and extreme pressure is fundamentally difficult to address theoretically. It is a dynamic, strongly correlated, partially degenerate composite of H_2, H, H^+, and electrons as well as other components, such as H_3, where no simple approximation is available.

Accurate knowledge of the thermodynamic properties of dense fluid hydrogen isotopes is required for demonstrating inertial confinement fusion (ICF) in the laboratory.[5] In the initial stages of an ICF implosion, a layer of deuterium–tritium (DT) fuel is compressed and accelerated through a sequence of progressively stronger shocks with amplitudes from around 80 to 5000 GPa (0.8 to 50 Mbar). Design of this hydrodynamic process critically depends on the high-pressure equation of state (EOS) of the DT fuel. Figure 1a shows a diagram of the principal Hugoniot[6] calculated from an established and widely used theoretical model (SESAME)[7] and the Hugoniot prediction from a more recent theory by Ross.[8,9] The more recent theory predicts a substantially higher density for shock amplitudes around 100 GPa. Fuel compression and acceleration begins with a single shock around 80 GPa. Subsequent shocks compress and accelerate the fuel further beginning from thermodynamic states originating along the single shock compression curve, i.e., the principal Hugoniot. The initial 80-GPa shock amplitude is situated in the region of greatest theoretical uncertainty in our understanding of the hydrogen EOS. This uncertainty produces practical consequences for ICF capsule design. For example, the additional compression around 100 GPa predicted with the recent Ross theoretical model influences the subsequent compression history of the fuel layer enough to lead to significantly different (higher) predictions of the capsule yield. Thus, accurate knowledge of the EOS of hydrogen is of considerable practical importance for ICF.

Evaluation of the competing theoretical models requires new experimental data along the principal Hugoniot into the few-100-GPa regime. In addition to the ICF application, the metallic transition and its effects on the EOS at pressures near 100 GPa are integral to models of many hydrogen-bearing astrophysical objects,[10] including Jovian planets,[11] extrasolar giant planets,[12] brown dwarfs,[13,14] and low-mass stars.[15] Figure 1b shows the phase space of hydrogen[16] in the vicinity of the finite-temperature, insulator–metal transition; its location relative to the principal shock Hugoniot; and the compression isentropes of Jupiter and Saturn. This region of phase space is experimentally accessible

*Department of Physics and Astronomy, University of British Columbia, Vancouver, Canada

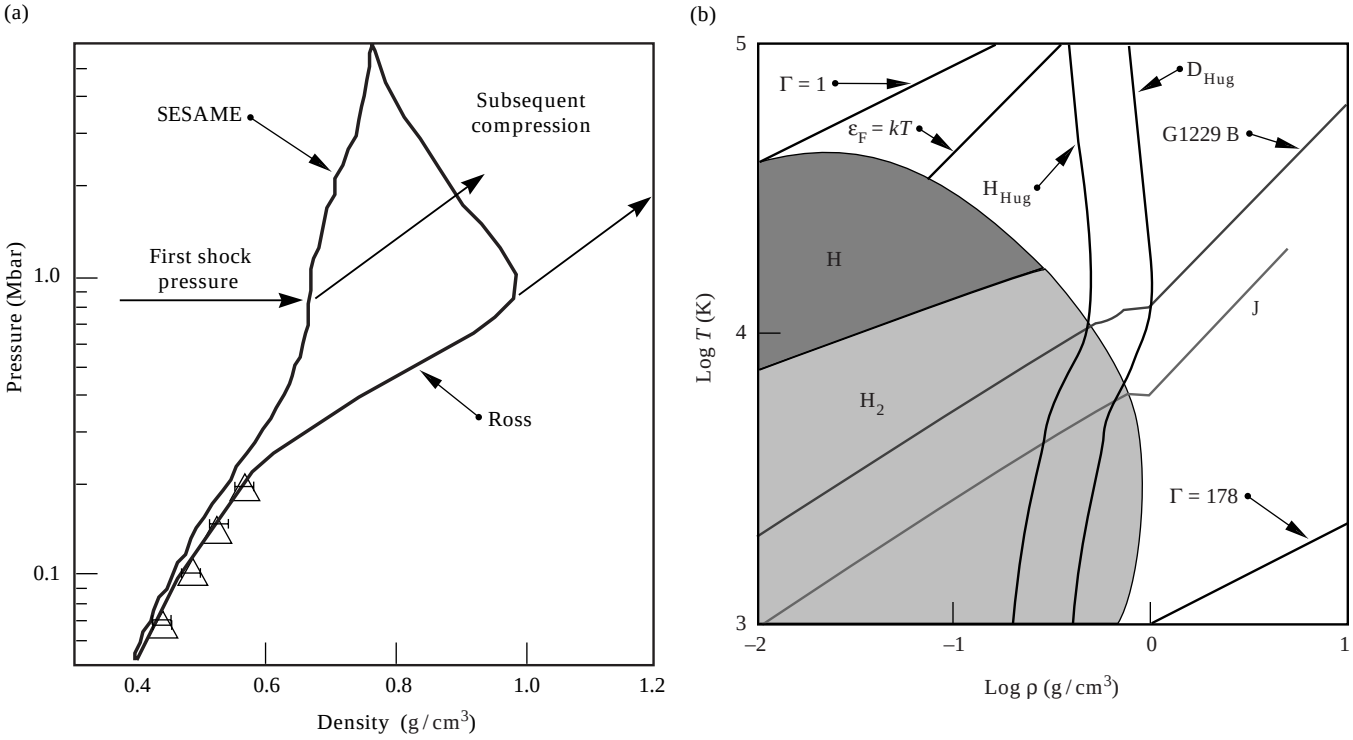

FIGURE 1. (a) Theoretical shock Hugoniot curves and initial paths for subsequent compression. The large, principal Hugoniot compression predicted by Ross implies that the fuel layer is compressed 50% more than that obtained from earlier models. The triangular points represent shock data from gas-gun experiments carried out in the 1980s. (b) Model phase diagram of hydrogen[16] in the regime of the fluid-metal–insulator phase transition. $\Gamma = e^2(4\pi/3n)^{1/3}/kT$ is a measure of the interparticle correlation strength, where n is the particle density; a value of $\Gamma > 1$ signifies strong coupling between the fluid constituents and a commensurate lack of simplifying assumptions that enable theoretical calculations. The Fermi energy is ε_F; for temperatures $kT < \varepsilon_F$, matter is partially degenerate. The regions identified as H_2 and H are mainly molecular and atomic hydrogen respectively; outside these regions, hydrogen is primarily an ionized fluid. "J" is a model isentrope for Jupiter; "G1229 B" is an isentrope for brown dwarf G1229 B.[14] "H_{Hug}" and "D_{Hug}" are model hydrogen and deuterium Hugoniots.[6,9] (50-00-1198-2192pb01)

from the principal shock Hugoniot, but meaningful measurements along the Hugoniot in this regime have, until recently, been unattainable due to lack of a sufficiently powerful shock driver. Using the Nova laser at Lawrence Livermore National Laboratory, we have accessed this regime by shocking liquid D_2 to pressures at and above the metallic transition, where we measured the thermodynamic properties of the shocked state.

At high pressures, both molecular dissociation and ionization can be activated through high-density as well as thermal effects. Early EOS models either did not include these effects or predicted that their consequences for the EOS would be small.[7,17] More recent theories predict that significant modifications to the EOS can occur either through a continuous dissociative transition[8,9] or a first-order phase transition[18–20] from the molecular to the metallic phase. In view of this theoretical situation, reliable experimental data have become valuable as a guide to theory. Shock-wave experiments using light gas guns have produced Hugoniot data on D_2 (initial density $\rho_0 = 0.17$ g/cm^3) up to 23 GPa ($\rho = 0.58$ g/cm^3 and $T = 0.39$ eV), below the transition.[8,21] Recently, radiographic measurements were made on the Hugoniot of liquid deuterium near 100 GPa employing a strong shock driven by an intense laser beam.[22] The few data indicated that the shock density of the isotopes at 100 GPa was much greater than had been predicted by established EOS theories.[7,17] The reason was attributed to the effects of high-density-produced molecular dissociation.[22]

Here, we report further measurements on the deuterium EOS, which extend the earlier compression data. In addition to our principal x-radiographic diagnostic, we have measured shock velocity and shock-front reflectivity with an optical probe, and thereby have obtained independent measurements of the shock trajectories. The new data set, obtained with two independent diagnostics, is internally self-consistent and corroborates the earlier data. We have also observed high optical reflectivities, characteristic of metallic conduction. This observation further corroborates the recent model predictions that the high compressibility is accompanied by transformation of the fluid into a conducting state.

Laser-Driven Shock Experiment

We used the Nova laser[23] to shock liquid deuterium to pressures between 22 and 340 GPa, which is a wider range of pressure than that in earlier experiments. In addition, we verified that this range spans the metal–insulator phase boundary. For each experiment, the shock wave pressure P and density ρ were determined from measurements of the shock speed U_s and the particle velocity behind the shock U_p using the Hugoniot relations $P = \rho_o U_s U_p$ and $\rho = \rho_o U_s/(U_s - U_p)$. Liquid D_2 at 20 K was contained in a 1.5- or 1.0-mm-diam, 0.45-mm-long cylindrical cell machined into a Cu block, as shown in Figure 2. One end of the cell was sealed with an Al or Be disk that acted as a pusher; the outside of each pusher was coated with 20 μm of either a polystyrene or Be ablator. The pushers were 180 to 250 mm thick with an rms surface roughness of 30 nm for Al and 90 nm for Be. X-ray-transmitting windows consisting of 5-μm-thick Be foils allowed us to perform radiography transverse to the shock direction through the sides of the cell. We also viewed the sample from behind through a 0.5-mm-thick sapphire window. A spatially smoothed Nova laser beam ($\lambda_L = 527$ nm) with an intensity of 10^{13} to 3×10^{14} W/cm^2 irradiated the ablator for 5 to 10 ns. The ablator served to minimize production of high-energy x rays in the laser plasma. Several laser-spot-size configurations were used over the course of the shots, from a 400- × 600-μm elliptical spot to a 1-mm-diam circular footprint. The rapidly heated ablator drove a shock wave into the metal pusher. Ideally, when the shock wave reached the rear of the pusher, the pusher–D_2 interface released into the D_2 at the speed U_p while the shock wave propagated ahead at the speed U_s.

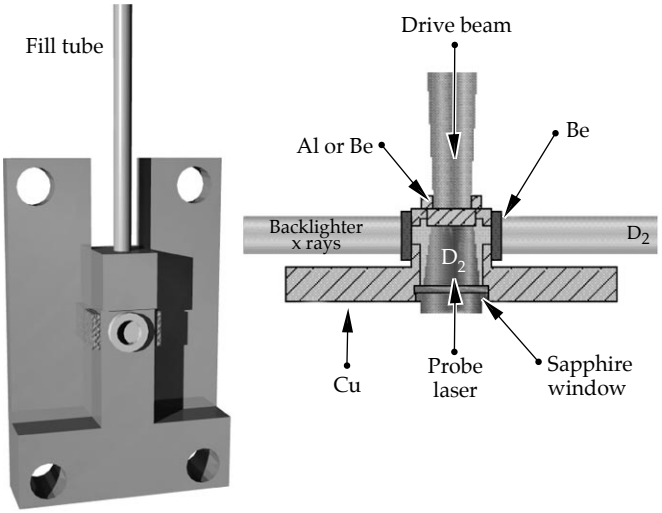

FIGURE 2. Sketch of the cryogenic cell used to contain the sample for the experiment. X-ray-transparent beryllium windows on the sides allowed for side-on x-ray shadowgraphic probing of the shock front. A probe beam transmitted through the rear sapphire window allowed for optical probing of the shock front. (50-00-1198-2193pb01)

X-Ray Radiography

Using transverse radiography, we tracked the positions of the shock front and the pusher–D_2 interface as a function of time to obtain measurements of U_s and U_p for each experiment. The radiography source was a laser-heated Fe foil located 12 cm from the cell. X rays from the Fe backlighter passed through the cell and into a Kirkpatrick–Baez microscope (bandpass of 800 ± 50 eV) and then into a streak camera. The streak camera slit subtended a strip 300 μm long by 5 μm wide at the target. The slit image was magnified 82 times with a spatial resolution of 3 μm at the object plane. 2D hydrodynamic simulations showed that edge rarefactions would attenuate the shock wave around its periphery. However, the simulations indicated that the shock wave would remain spatially uniform and temporally steady in the center of the shock wave for sufficient time to obtain accurate data.

The earlier experiments used only Al pushers to obtain a maximum pressure of 210 GPa (Ref. 22). Here, we extended the measurements to higher pressure using Be pushers, which have a lower density than Al. The significance of higher pressure is that on the Hugoniot above the metal–insulator transition regime, the compression must eventually approach a value of four.[6] Failure to exhibit this effect would call the experimental methodology into question. Because Be is relatively transparent to keV-energy x rays produced in the laser plasma (and thus more likely to allow preheating of the D_2 sample), we inserted an x-ray-blocking layer of 1-μm-thick Au between the ablator and pusher. The Au did prevent preheating of the D_2, but it also caused shock-wave reverberations in the pusher that were not completely damped by the time the shock wave released into the D_2. The higher-pressure shock waves achieved using Be exhibited more temporal variation immediately after release than those produced with Al, resulting in larger uncertainties in measurements of U_s and U_p.

Figure 3 shows a streak radiograph of shock-compressed D_2 with a Be pusher. The pusher is opaque to backlighter x rays, so the interface is the boundary between the light and dark regions. At $t = 0$, the shock wave crosses the interface, and the interface surface begins to move. By 3 ns, the interface is moving at the final speed U_p. Grazing incidence refraction of the backlighter at the density jump across the shock front

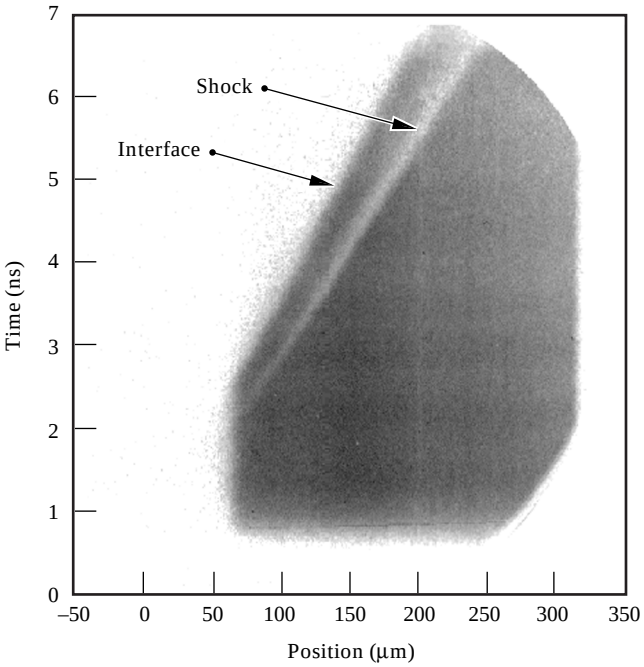

FIGURE 3. Transverse streak transmission radiograph of a D_2 EOS target with a Be pusher at a laser intensity of 7.6×10^{13} W/cm^2. Shock release into the D_2 is at $t = 0$. The image shows a shock decelerating until $t = 3$ ns, at which time it becomes steady where the slopes of the interface and shock are U_p and U_s, respectively. (50-00-1198-2194pb01)

occurs at angles larger than the acceptance angle of the microscope, so that the shock front is visible as a dark line propagating ahead of the interface. The slope of this line is U_s. Absolute uncertainties in U_s and U_p were determined from uncertainties in sweep speed (0.3%), magnification (0.5%), and point selection and deviation of the trajectories from linearity (1%).

Velocity Interferometry

The sapphire window at the back of the cell admitted a probe laser. In the original experiments,[22] the probe was used in a Michelson interferometer configuration, imaging the rear of the pusher through the unshocked D_2. The interferometer monitored the surface position for evidence of radiative heating of the target. The demonstrated lack of sample preheat allowed us to use laser-driven shock waves for EOS measurements.[24]

For these experiments, the probe laser ($\lambda_P = 1.064$ μm) was used for velocity interferometry, a technique that measures the Doppler shift of light reflected from a moving surface.[25,26] This kind of experimental arrangement is a standard tool available at many shock research facilities and is known as a velocity interferometer system for any reflector (VISAR). The reflected beam was imaged onto the slit of a streak camera after passing it through the interferometer. The recorded fringe shift is directly proportional to the Doppler shift and, therefore, to the velocity of the reflecting surface. Figure 4a shows an example recording of a streaked interferogram from our VISAR system. This particular experiment intentionally produced a decaying shock that decelerated as it propagated. For negative times on the scale in Figure 4a, the recording shows the reflection from the Al pusher surface prior to the emergence of the shock into the deuterium sample. For positive times, light was reflected from the shock front. The drive-beam focal spot was slightly nonuniform, and therefore produced a spatial variation in the breakout time at the pusher–deuterium interface, which is readily observable in the image. When the shock emerged from the Al interface, the reflected intensity dropped simultaneously with a shift of the fringe pattern.

Figure 4b shows the spatial variation of the fringe intensity across the target at a single moment around $t = 2$ ns during the experiment. We extract ϕ from a fit of the observed fringe intensity I to a sinusoidal function: $I(x,t) = A(x,t) + B(x,t) \sin \phi\,(x,t)$. The measured velocity[25] is $U_s = \lambda_P \phi(t) / 4\pi\tau(1 + \delta)$, where τ (= 75 ps) is a delay time set by the configuration, $\phi(t)$ is the phase, and δ is a small correction associated with the interferometer.

Figure 4c shows how the fitted fringe phase varies with time in the center of the recorded image. From these data, we obtain a continuous record of phase, and therefore shock velocity as a function of time. The initial phase shift at $t = 0$ is ambiguous because the streak camera cannot resolve the fringe motion quickly enough during the 75 ps (τ) in which the fringes shift to the new phase. A shift of one fringe is 7 μm/ns with a resolution of <0.1 fringe. With high sensitivity, the initial shift can be several fringes, whereas the recording determines only the fractional part of the fringe shift. We resolved the ambiguity by comparing the velocimetry data with the radiograph of the shock trajectory. At shock breakout, the raw phase shift was -0.23 ± 0.05 fringes; the true phase shift was 2.77 ± 0.05 fringes, giving a shock speed of 18.9 ± 0.3 km s^{-1}. In the absence of an independent diagnostic, this ambiguity can also be resolved by splitting the reflected light and recording data from two velocity interferometers with different sensitivities.

In Figure 5, we have integrated the extracted velocity to determine the shock trajectory (position as a function of time). We compare this with a streaked radiograph of the shock trajectory recorded simultaneously. Both trajectories agree within the ±3-μm uncertainty of the radiographic measurement. In this example, the position inferred from the VISAR record after 6 ns is more accurate (we

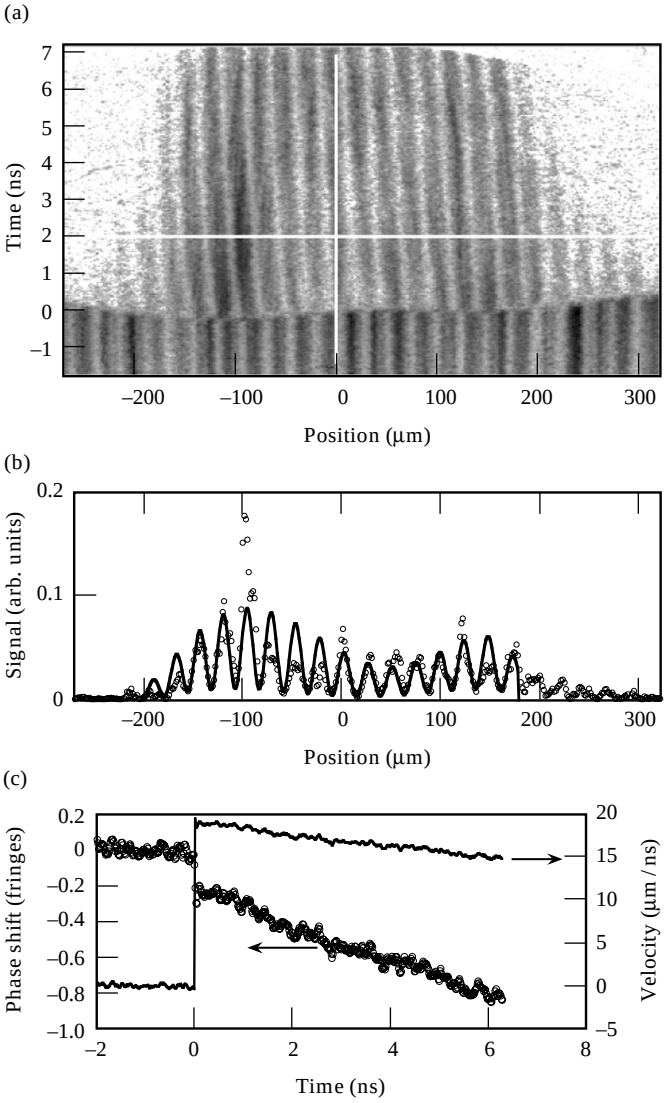

FIGURE 4. (a) Example of a streaked VISAR interferogram recorded for a decaying shock front. The initial phase shift is 2.77 fringes to the right, followed by a continuous shift to the left (deceleration) of ~0.7 fringes after 6 ns. (b) Interferogram intensity as a function of position x measured (symbols) and fitted (curve) at $t = 2$ ns [see the horizontal line in (a)]. (c) Raw phase at $x = 0$ (open circles) extracted from a series of fits similar to (b) for all times, and velocity (solid curve) obtained after applying an integer offset of +3 fringes to the raw phase data. The initial phase offset for $t < 0$ was subtracted. (50-00-1198-2195pb01)

estimate about ±0.2 μm) because the integration averages out random fluctuations in the phase, leaving systematic errors as the dominant contribution. This measurement also confirms unambiguously that the Doppler-shifted optical reflection originated directly from the shock front. Other possible choices for the initial fringe offset (e.g., 1.77 or 3.77 fringes) do not produce trajectories that correlate with any other moving surface or interface in the experiment.

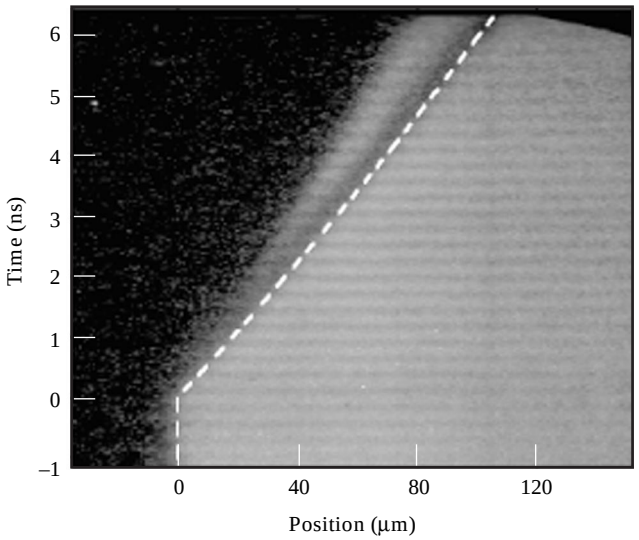

FIGURE 5. Streaked radiograph of the propagating shock front measured simultaneously with the record in Figure 4. The dashed curve shows the trajectory calculated from the measured velocity record in Figure 4c by integrating the velocity. The trajectory inferred from the velocity measurement lies within the resolution limit of the radiograph (±3 μm) for the entire trajectory in the recording (up to 6 ns). (50-00-1198-2196pb01)

The agreement between two completely independent experimental techniques strengthens our confidence in the validity of the data produced by either diagnostic.

Optical Reflectivity

In addition to U_s, the interferometer also supplied instantaneous measurements of the (single-wavelength) reflectivity of the shock front. The optical reflectivity as a function of shock amplitude at the probe wavelength, 1064 nm, is plotted in Figure 6. At low shock pressures (20 GPa), the reflectivity is a few percent. However, at pressures greater than 55 GPa, the measured reflectivities are around 60%, characteristic of a metal. Because the temperature of the shocked D_2 is ~0.75 eV, much less than the ionization potential, the high reflectivity must be due to free electrons produced by a combination of density and thermal effects. The temperature is much less than the Fermi energy ε_F (~15 eV), so that the electron fluid is Fermi-degenerate. Because of this fact, the velocity distribution of the charge carriers depends mainly on density, and electron conduction is weakly temperature dependent. In plasma physics, such an ionization mechanism is referred to as pressure ionization. With respect to condensed matter terminology, ionized fluids with Fermi-degenerate conducting electrons are usually referred to as liquid metals. This is the most appropriate term to describe the high-pressure ionized fluid at pressures greater than 55 GPa.

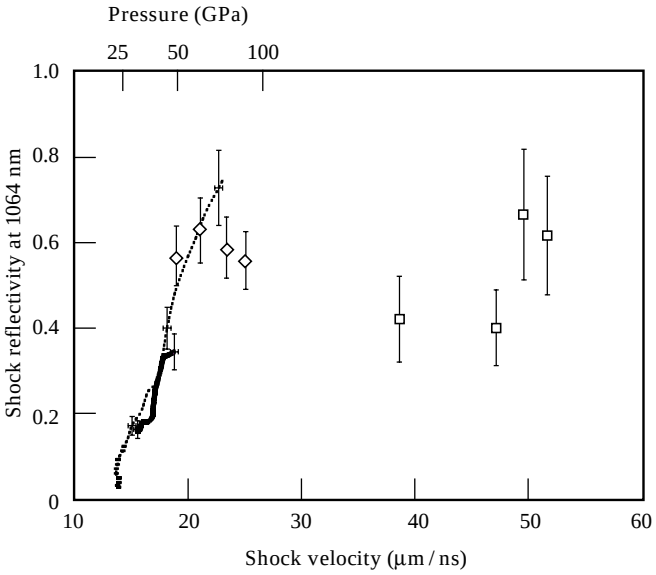

FIGURE 6. Reflectivity at 1064 nm of the shock front in liquid deuterium for shock speeds from 13.4 to 53 μm/ns. The open symbols are single-point measurements observed at the moment of shock breakout from the pusher–deuterium interface: diamonds are from experiments with Al pushers, squares are with Be pushers. The solid curves were extracted from two decaying-shock experiments. Indicated pressures were determined from Hugoniot data.[22] (50-00-1198-2197pb01)

Shock Compression Results

At the lowest compression, the laser data agree with gas-gun results[8,21] (Figure 7). The most striking feature is the pronounced compressibility observed at the same pressure at which D_2 becomes metallic. At 100 GPa, the SESAME[7] D_2 Hugoniot density is 0.68 g/cm^3 ($\rho/\rho_0 = 4$), whereas the data show a density of 1.0 g/cm^3 ($\rho/\rho_0 = 5.88$), an increase of 47%. The softer EOS is similar to the models of Saumon–Chabrier[16,18] and Ross.[8,9] All of these models use minimization of the free energy of a mixture of molecular, atomic, and ionic species to determine species concentrations and establish the thermodynamics of the mixture. The methods, and in particular the interspecies potentials, are different in each case. Ross uses the expedient of a term determined by gas-gun shock-wave data. The Monte Carlo simulations[19] are the closest to *ab initio*, i.e., an integration of the interactions of a finite set of individual nuclei and electrons. They show a high compression but at a low pressure. The high-temperature ACTEX model[27] also predicts a high shock density. However, the paths to higher pressure of these latter models lie to the low-density side of the data. A Hugoniot calculated from data produced by tight-binding molecular dynamics,[28] like SESAME, predicts only slight effects of dissociation and ionization.

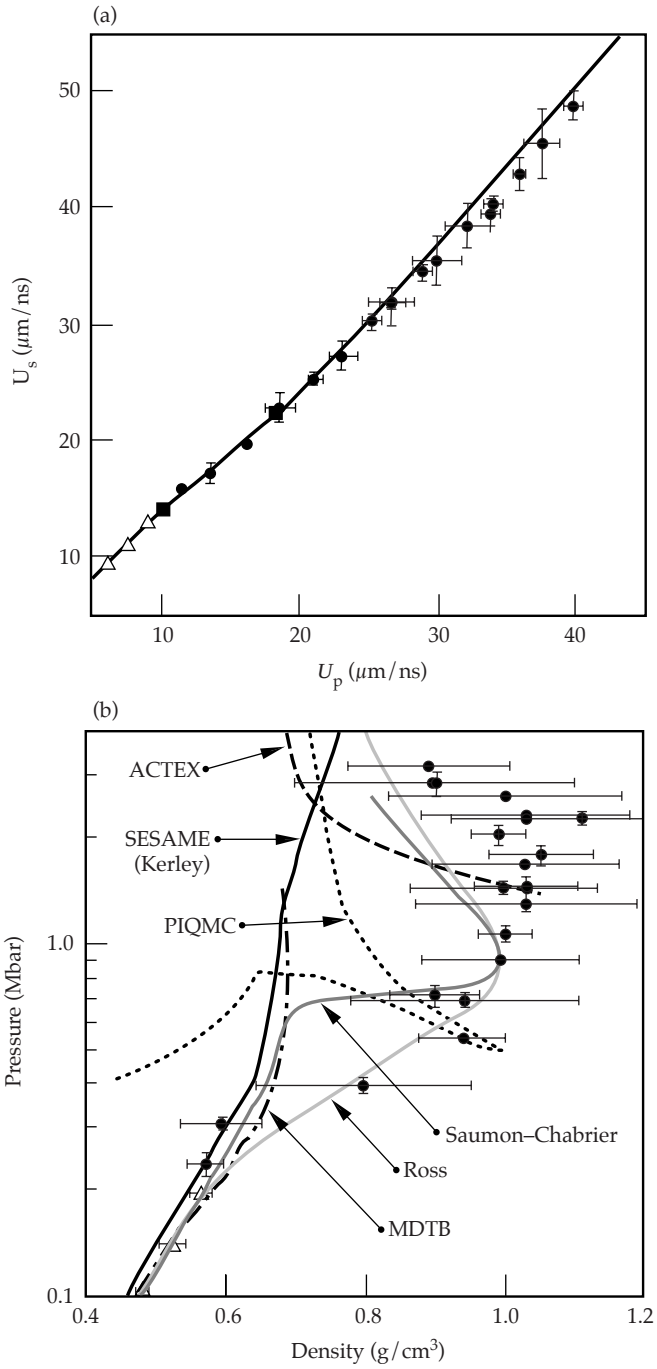

FIGURE 7. Hugoniot data presented as (a) measured U_s vs U_p and (b) inferred pressure vs density. Gas-gun data (triangles) are shown.[8,21] The EOS model of Ross[8,9] is shown as the light gray line. Other theoretical Hugoniots in (b) are from the widely used SESAME tabular EOS (black solid),[7] the hydrogen EOS of Saumon and Chabrier that is used extensively in modeling of low-mass stellar objects (gray),[16] the ACTEX theory that is known to be accurate at high temperatures (dash),[27] path integral quantum Monte Carlo simulations (dots),[19] and tight-binding molecular dynamics simulations (dot dash).[28] (50-00-1198-2198pb01)

Above the turnaround on the Hugoniot, D_2 is a fully dissociated, partially ionized metallic fluid, so that as the pressure increases, the shock density is expected to move closer to that of an ideal gas.[6] This trend was unclear in the original experiments. Here, the compression data above 200 GPa show a trend toward the ideal gas compression (Figure 7b).

Summary

Our data offer an independent assessment of the EOS of hydrogen isotopes on both sides of the metal–insulator phase transition. We have shown that hydrogen is ~50% more compressible at the transition than some theories predict.[7,17,28] The question remains as to whether this transition is continuous. The flattened Hugoniots for two EOS models[18,19] are the result of the Hugoniot passing through a predicted first-order phase transition from the molecular to the metallic state (Figure 7b). The other methods assume a continuous transformation. There is no evidence in the Hugoniot data for a first-order phase transition; both shock trajectories and reflectivity display a continuous variation from 25 to 70 GPa. Although there are significant uncertainties in the data, they suggest that the metal–insulator transition is continuous along the Hugoniot.

Acknowledgments

The authors thank N. W. Ashcroft, D. M. Ceperley, G. Chabrier, Y. M. Gupta, A. U. Hazi, N. C. Holmes, J. D. Johnson, G. I. Kerley, W. J. Nellis, M. Ross, F. J. Rogers, D. Saumon, T. Tajima, and D. A. Young for highly informative discussions and J. R. Asay, B. A. Hammel, J. D. Kilkenny, and L. G. Wiley for advice and support.

Notes and References

1. N. W. Ashcroft, *Phys. World* **8**, 43 (July, 1995).
2. E. Wigner and H. B. Huntington, *J. Chem. Phys*. **3**, 764 (1935); C. Friedli and N. W. Ashcroft, *Phys. Rev. B* **16**, 662 (1977); T. W. Barbee et al., *Phys. Rev. Lett*. **62**, 1150 (1989); H. Chacham and S. G. Louie, *Phys. Rev. Lett*. **66**, 10963 (1991).
3. J. H. Eggert et al., *Phys. Rev. Lett.* **66**, 671 (1991); C. Narayana, H. Luo, J. Orloff, and A. L. Ruoff, *Nature* **393**, 46 (1998).
4. S. T. Weir, A. C. Mitchell, and W. J. Nellis, *Phys. Rev. Lett.* **76**, 1860 (1996).
5. S. W. Haan et al., *Phys. Plasmas* **2**, 2480 (1995); J. D. Lindl, *Phys. Plasmas* **2**, 3933 (1995); S. Nakai and H. Takabe, *Rep. Prog. Phys.* **59**, 1071 (1996).
6. The Hugoniot is the locus of density, pressure, and energy states in a material following passage of a single shock. It is a well-defined curve on the EOS surface. The compression (ratio of shocked to unshocked density) generally increases with pressure and approaches a value of 4 for an ideal gas in the high-pressure limit. The ratio can be greater than 4 when accounting for endothermic processes, such as molecular excitations, dissociation, or ionization. At pressures above the region where these processes are complete, the compression must approach the ideal gas limit. EOSs for hydrogen isotopes are identical, except for a scale factor in density.
7. G. I. Kerley, *A Theoretical Equation of State for Deuterium*, Los Alamos National Laboratory, Report LA-4776 (1972); G. Kerley, *J. Chem. Phys*. **73**, 460 (1980).
8. N. C. Holmes, M. Ross, and W. J. Nellis, *Phys. Rev. B* **52**, 15835 (1995).
9. M. Ross, *Phys. Rev. B* **58**, 669 (1998).
10. H. M. Van Horn, *Science* **252**, 384 (1991).
11. R. Smoluchowski, *Nature* **215**, 691 (1967); W. B. Hubbard, *Science* **214**, 145 (1981); G. Chabrier, D. Saumon, W. B. Hubbard, and J. I. Lunine, *Astrophys. J*. **391**, 817 (1992); W. J. Nellis, M. Ross, and N. C. Holmes, *Science* **269**, 1249 (1995).
12. D. Saumon et al., *Astrophys. J*. **460**, 993 (1996).
13. D. Saumon, W. B. Hubbard, G. Chabrier, and H. M. Van Horn, *Astrophys. J*. **391**, 827 (1992).
14. W. B. Hubbard et al., *Phys. Plasmas* **4**, 2011 (1997).
15. G. Chabrier and I. Baraffe, *Astron. Astrophys*. **327**, 1039 (1997).
16. D. Saumon, G. Chabrier, and H. M. van Horn, *Astrophys. J. Suppl. Ser*. **99**, 713 (1995).
17. M. Ross, F. H. Ree, and D. A. Young, *J. Chem. Phys*. **79**, 1487 (1983).
18. D. Saumon and G. Chabrier, *Phys. Rev A* **44**, 5122 (1991); *Phys. Rev A* **46**, 2084 (1992); *Phys. Rev. Lett*. **62**, 2397 (1989).
19. W. R. Magro, D. M. Ceperley, C. Pierleoni, and B. Bernu, *Phys. Rev. Lett*. **76**, 1240 (1996); B. Militzer, W. Magro, and D. Ceperley, *Proc. International Conf. Strongly Coupled Coulomb Systems*, G. J. Kalman, K. B. Blagoev, and J. M. Rommel, Eds. (Plenum, New York, 1998).
20. H. Reinholz, R. Redmer, and S. Nagel, *Phys. Rev. E* **52**, 5368 (1995).
21. W. J. Nellis et al., *J. Chem. Phys*. **79**, 1480 (1983).
22. L. B. Da Silva et al., *Phys. Rev. Lett.* **78**, 483 (1997).
23. E. M. Campbell, *Laser Part. Beams* **9**, 209 (1991).
24. Y. M. Gupta and S. M. Sharma, *Science* **277**, 909 (1997).
25. L. M. Barker and R. E. Hollenbach, *J. Appl. Phys*. **43**, 4669 (1972).
26. P. M. Celliers et al., *Appl. Phys. Lett.* **73**, 1320 (1998)
27. F. J. Rogers, *Astrophys. J*. **310**, 723 (1986); F. J. Rogers, F. J. Swenson, and C. A. Iglesias, *Astrophys. J*. **456**, 902 (1996).
28. T. J. Lenosky, J. D. Kress, and L. A. Collins, *Phys. Rev. B* **56**, 5164 (1997).